Optik - International Journal for Light and Electron Optics 227 (2021) 165520

Contents lists available at ScienceDirect

Optik

journal homepage: www.elsevier.com/locate/ijleo

Original research article

Posture optimization of a 3-6R parallel mechanism for secondary mirror truss applied on large telescopes

Rui Wang [a,b], Fuguo Wang [a,*], Liang Hao [a], Yuyan Cao [a], Xueqian Sun [a,b]

[a] *Changchun Institute of Optics, Fine Mechanics and Physics, Chinese Academy of Sciences, Changchun, 130033, China*
[b] *University of Chinese Academy of Sciences, Beijing 100049, China*

ARTICLE INFO

Keywords:
Posture optimization
Wavefront aberration
Stiffness performance index
Truss mechanism
Large aperture telescope

ABSTRACT

The traditional truss structure adopts a fixed form, which is the main reason for the over-height of the vehicle telescope. In order to achieve larger vehicle-mobile telescopes and solve the over-height problem, the new truss mechanism based on robotics is proposed in this paper. Based on the new structure, the posture and dimension parameters need to be determined. Stiffness has great effects on accuracy and resonance of the telescope system, which is influenced by the posture and dimension parameters. So the stiffness performance index is used to optimize the posture. Meanwhile, in order to simulate the force of the telescope in different states, translation evaluation index (TEI) and rotation evaluation index (REI) are represented in this paper. Wavefront aberrations can be obtained by establishing the relationship between TEI, REI and Zernike polynomials. The optimized posture is verified to meet the error requirement through this method and the accuracy is obviously improved through comparison.

1. Introduction

Telescopes can either be fixed stationary or movable. Vehicle-mobile telescopes have a great advantage over ground-based telescopes in terms of mobility and efficiency. From Rayleigh criterion, it can be known that angular resolution of optical instruments is $\theta = 1.22\lambda/d$, which means the telescope can get higher resolution if the diameters are larger [1]. However, it is impossible to transport large telescopes by road as they do not meet height requirements of bridges and culverts. Therefore, vehicle-mobile telescopes remain in the scale of 1 m, which restricts the development of their diameter. Thus, the author proposed the new truss structure based on robotics in parallel instead of the traditional Serrurier truss to reduce the altitude. The diameter of the telescope can be raised to 2 m scale.

Secondary mirrors are generally fixed to the telescope by Serrurier truss as the supporting component, and a secondary mirror assembly is installed above the Serrurier truss via Stewart platform, which adjusts the position of the mirror in six-dimensional motion [2–4]. The Serrurier truss accounts for about half of the total height of the telescope, which is the main reason for over-height of vehicle telescopes. This paper presents a structure of the truss mechanisms in the form of parallel robotic arms, which integrates the supporting part of the traditional Serrurier truss and the adjusting part of the Stewart platform.

When determining the structural form, symmetry and stability are important for a secondary mirror support system in a telescope. At the same time, it is necessary for the secondary mirror to have a five-dimensional motion in addition to the rotation along the z-axis.

* Corresponding author.
E-mail address: wfg109@163.com (F. Wang).

https://doi.org/10.1016/j.ijleo.2020.165520
Received 24 May 2020; Received in revised form 24 August 2020; Accepted 26 August 2020
Available online 23 November 2020
0030-4026/

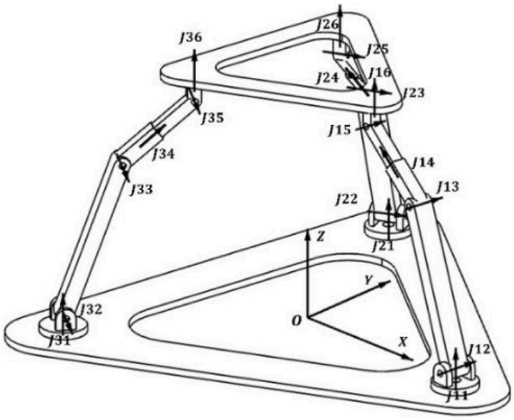

Fig. 1. Structure of parallel truss mechanism.

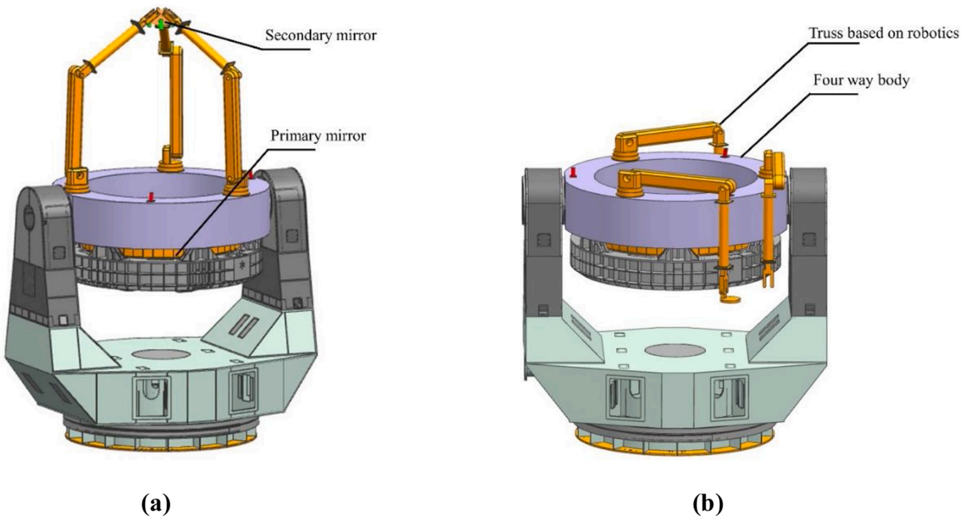

Fig. 2. Telescope based on robotics (a)working state (b)transportation state.

Therefore, the new truss takes the form of a symmetrical parallel mechanism. The stability can be promoted with more limbs but the overall weight will also increase. The number of joints on each limb will influence the resonance as well. So the number of joints and limbs should be minimized under the premise of system stiffness. The structure of 3-6R shown in Fig. 1 is adopted after calculation. It can meet the resonance frequency requirement and the five-dimensional adjustment movement of the secondary mirror truss system.

The structure shown in Fig. 2 is the 3-6R parallel mechanism meeting the DOF requirement of the secondary mirror. The new designed truss has both positioning and freedom adjustment functions. The relative position can be adjusted through the structure while the secondary mirror shifts. When the telescope is in operation, the secondary mirror assembly is placed at the specified position by the motion of the truss. When the telescope is not in operation or being transported, the secondary mirror assembly moves with the motion of the robotic arm, and the truss is placed on the side of the telescope. Thus, the over-height and diameter problems are solved by the new structure. The largest diameter of the vehicle-mobile telescope based on traditional structure is 1.2 m. The resolution can be increased by 1.7 times and the light collection capabilities can be increased by 2.8 times if the diameter is up to 2 m. So the new structure has a better optical performance. Meanwhile, changing secondary mirror will be easier if the movable truss is used.

Up to now, Similar structure only has been used by James Webber Space Telescope. The truss is folded in rocket when it's launching, and the truss opens up when it's in track. The foldable mechanism only has the rotation DOF. It can provide high accuracy positioning but it doesn't have the adjustment function. The truss integrated with positioning and adjusting functions has not appeared yet. The new designed truss takes account of image quality and mobility of the telescope, and the design has broad application prospects [5–7,27,28].

The relative position between the primary mirror (PM) and the secondary mirror (SM) is determined by the requirement of optical design, but the dimension parameters and the posture of the robotic truss are not determined. Posture design is basic and important in structure analysis, which influences the stiffness and the accuracy of the system. The relationship of input and output also changes in different postures [8–12]. Stiffness is a key index in telescope system design and has influences on resonance of the telescope system and rigid deformation error of the robotic truss. The stability is related to the resonance frequency and the wavefront aberration is related to the deformation. Thus, posture of the secondary truss mechanism is optimized based on stiffness index and verified by rigid deformation error in this paper [13–16].

2. Basic principles

2.1. Stiffness evaluation index

Stiffness and mass optimization of parallel mechanism has been studied in some researches. However, the symmetrical structure is usually used in the design of the telescope because of the high precision and symmetry requirement of the optical system, one limb is optimized in this paper instead of the parallel mechanism, and the parallel stiffness matrix is calculated after the optimization. The structure has the working mode and the transportation mode. The truss is locked on the side of the telescope and the telescope is not working during transportation. The posture in working mode is optimized in this paper.

In order to avoid the problem of singularity in the calculation of general stiffness model [17–19], the compliance matrix is adopted by Guo:

$$C = JK_\theta^{-1}J^T = \begin{bmatrix} C_{tt} & C_{tr} \\ C_{tr}^T & C_{rr} \end{bmatrix} \tag{1}$$

This avoids the inverse Jacobian matrix in the calculation. Compliance matrix C is divided into C_{tt}, C_{tr} and C_{rr} as 3×3 matrices. K_θ can be written as:

$$K_\theta = \begin{bmatrix} k_1 & 0 & \cdots & 0 \\ 0 & k_2 & \cdots & 0 \\ \vdots & \vdots & \ddots & \vdots \\ 0 & 0 & \cdots & k_6 \end{bmatrix} = \begin{bmatrix} K_{11} & K_{12} \\ K_{21} & K_{22} \end{bmatrix} \tag{2}$$

k_i indicates the i-th joint stiffness of the limb. K_θ is divided into 3×3 matrices as shown in Eq. (2) According to the compliance matrix, the stiffness evaluation index can be defined as [20–22]:

$$k_{stif} = \frac{1}{\sqrt[3]{\det(C_{tt})}} = \frac{1}{\sqrt[3]{\det(J_{11}K_{11}^{-1}J_{11}^T + J_{12}K_{22}^{-1}K_{12}^T)}} \tag{3}$$

J can be decomposed into J_{ii} and expressed as

$$J = \begin{bmatrix} J_{11} & J_{12} \\ J_{21} & J_{22} \end{bmatrix} \tag{4}$$

Therefore, the optimization of the robot posture can be regarded as the maximization of the stiffness index according to Eq. (3).

2.2. Translation evaluation index and rotation evaluation index

Since the orientation of the telescope changes during observation, the gravity of the secondary mirror changes as well. k_{stif} does not introduce the influence of a force or a torque, so it cannot be the only evaluation standard of posture optimization. However, the evaluation of the SM misalignment requires the analysis of compliance matrix and the force. So translation evaluation index (TEI) and rotation evaluation index (REI) are proposed in this paper to calculate the translational offset and rotational offset of the SM at different pitch angles of the telescope system. If w is the generalized displacement and Δx_g is the generalized force, the misalignment of the SM is:

$$\Delta x_g = Cw \tag{5}$$

Translational deformation corresponds to piston in optical system, rotational deformation along x-axis and y-axis corresponds to tip and tilt. Both need to be considered to analyze the wavefront aberrations. Since this structure is applied on the telescope system, the relationship between wavefront aberrations and deformation evaluation index need to be established through Zernike polynomials to evaluate the optical performance.

Then, Eq. (5) should be rewritten as:

$$\begin{bmatrix} \Delta x \\ \Delta \theta \end{bmatrix} = \begin{bmatrix} C_{tt} & C_{tr} \\ C_{tr}^T & C_{rr} \end{bmatrix} \begin{bmatrix} f \\ \gamma \end{bmatrix} = \begin{bmatrix} C_{tt}f + C_{tr}\gamma \\ C_{tr}^T f + C_{rr}\gamma \end{bmatrix} \Rightarrow \begin{cases} \Delta x = fC_{tt}e_f + \gamma C_{tr}e_\gamma \\ \Delta\theta = fC_{tr}^T e_f + \gamma C_{rr}e_\gamma \end{cases} \tag{6}$$

Δx and $\Delta\theta$ are translational and rotational deformation vectors separately; f and γ are force and torque vectors separately. Since the telescope's pitch angle changes slowly during operation, any working state can be regarded as static for analysis, so the truss mechanism is only influenced by the gravity of secondary mirror component. Thus, with consideration of the unit force and torque, TEI can be calculated as:

Table 1
First three Zernike polynomials.

j	n	m	Zernike polynomials $R_n^m(\rho,\varphi)$	Wavefront aberration
1	0	0	1	Piston
2	1	1	$\rho\cos\theta$	Tip
3	1	−1	$\rho\sin\theta$	Tilt

$$TEI = \frac{\Delta\overline{x}}{f} = \frac{\sqrt{(C_{tt}e_f)^T C_{tt}e_f}}{f} = C_{tt}e_f \tag{7}$$

Similarly, REI can be defined as:

$$REI = \frac{\Delta\overline{\theta}}{f} = \frac{\sqrt{(C_{tr}^Te_f)^T C_{tr}^Te_f}}{f} = C_{tr}^Te_f \tag{8}$$

The optimized compliance matrix is calculated in Eqs. (7) and (8) to obtain the influence of the SM misalignment on the wavefront aberration and verify whether it meets the system requirements.

2.3. Wavefront aberrations expressed by Zernike polynomials

Zernike polynomials are orthogonal basis expressed with polar coordinates in the unit circle. Zernike polynomials with different symmetry correspond to wavefront aberrations caused by the telescope system [23,24].

Zernike polynomials are expressed as

$$R_j(\rho,\varphi) = R_n^m(\rho,\varphi) \tag{9}$$

The relationship between Zernike series j and m, n in the function is

$$b = ceil\sqrt{j} \tag{10}$$

$$a = b^2 - j + 1 \tag{11}$$

$m = -\frac{a}{2}$, a is even; $m = \frac{a-1}{2}$, a is odd (12)

$$n = 2(b-1) - |m| \tag{13}$$

First three Zernike polynomials shown in Table 1 are considered in this paper.

3. Posture optimization

The stiffness performance of the robot is influenced by the robot posture and dimension parameters. Due to the relative position between PM and SM is determined, the dimension is changing when the posture is optimized. So both should be considered in optimization. The method adopted in this paper is establishing the relationship between the stiffness coefficient and the parameters of the truss and set the stiffness coefficient as the objective function. In the process of solving the maximum stiffness coefficient, the optimal posture and dimension parameters are solved [25]. The optimization process is shown as follows: First, the joint stiffness is determined before optimization. Second, Dimension limitation is added while optimizing J2 and J3 to meet the relative position between PM and SM. Finally, Maximum stiffness performance index is solved by adjusting each joint angle and the parameter of each link.

3.1. Posture optimization by stiffness evaluation index

Since the secondary mirror is connected at the end of the robotic arm, the misalignment of the secondary mirror can be regarded as the translational deformation and rotational deformation of the end effector, and it can be expressed as

$$\begin{bmatrix}\Delta x\\ \Delta\theta\end{bmatrix} = \begin{bmatrix}C_{tt}f\\ C_{tr}^Tf\end{bmatrix} = \begin{bmatrix}C_{tt}\cdot f\cdot e_f\\ C_{tr}^T\cdot f\cdot e_f\end{bmatrix} \tag{14}$$

Due to e_f is the direction vector of the force, The pitch motion of the telescope can be simulated by adjusting e_f. According to Eqs. (1) and (14), for a certain pitch angle, the secondary mirror misalignment is only determined by the Jacobian matrix. In order to obtain the ideal secondary mirror misalignment by the optimal Jacobian matrix, we established the coordinate system of each joint for the selected manipulator as shown in Fig. 3. Then, the Denavit-Hartenberg parameters (DHm) can be obtained as shown in Table 2.

From Eq. (1) and the parameters in Table 2 we can see the objective function k_{stif} is influenced by θ_i, a_i and d_i.Due to the method of

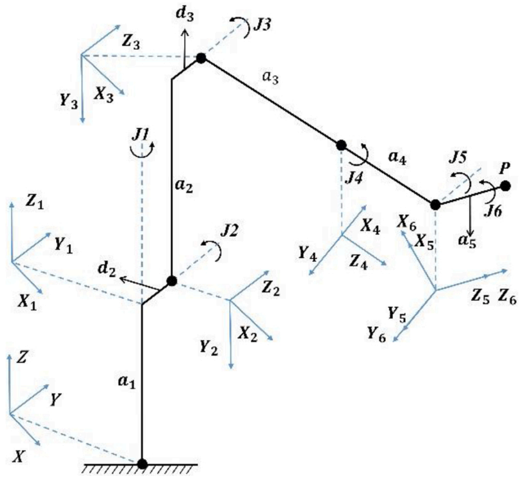

Fig. 3. DHm parameterization of the limb and the position of joints.

Table 2
DHm parameters of the limb and the position of joints.

	J1	J2	J3	J4	J5	J6
$\theta_i(rad)$	θ_1	θ_2	θ_3	θ_4	θ_5	θ_6
$\alpha_i(\deg)$	-90°	0°	-90°	90°	-90°	0°
$a_i(mm)$	a_1	a_2	a_3	a_4	a_5	0
$d_i(mm)$	0	d_2	d_3	0	0	0

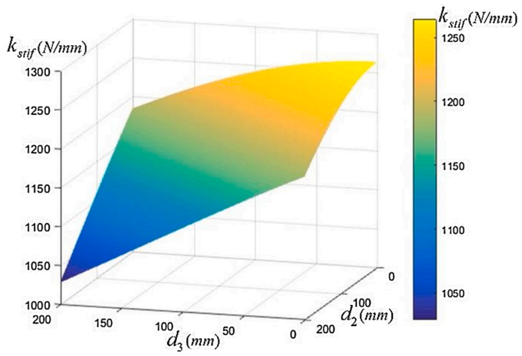

Fig. 4. optimization of d_2 and d_3.

coordinate establishment in Fig. 3, SM is connected with EE at point P, so θ_1, θ_6, a_6 doesn't influence k_{stif}. θ_4 is set to 0 in order to make the z-axis of PM and SM is coaxial, then θ_4 is determined. Thus, k_{stif} is influenced by θ_2, θ_3, θ_5, d_2, d_3, a_1 - a_5.

In addition, Joint stiffness must be determined before optimization. Owing to the constraints of the relative position between the PM and SM, we selected the Smart5 NJ 220−2.7 robot, so K_θ is $[1.5727 \times 10^9, 6.7566 \times 10^9, 1.1169 \times 10^9, 3.3249 \times 10^8, 1.1038 \times 10^8, 4.1444 \times 10^8](N \cdot mm/rad)$ [26].

Yang Lin et.al found that the EE position is influenced by J2-J3 mostly and the orientation is affected by J4-J6 [26]. In order to meet the requirement of relative position between PM and SM, space constraints is added by J2 and J3.So a_2 and θ_2 should be optimized at the same time, so does a_3 and θ_3.

The initial values of the parameters are shown as follows:

$\theta_1 = 0$, $\theta_2 = 0$, $\theta_3 = 0$, $\theta_4 = 0$, $\theta_5 = \frac{\pi}{4} rad$, $\theta_6 = 0$, $d_2 = 200mm$, $d_3 = 200mm$, $a_1 = 200mm$ $a_2 = 1320mm$, $a_3 = 800mm$, $a_4 = 500mm$, $a_5 = 200mm$

3.1.1. Optimization of d_2 and d_3

Fig.4 shows the influence of stiffness index caused by d_2 and d_3. Other parameters are determined, d_2 and d_3 are adjusted from 0 to

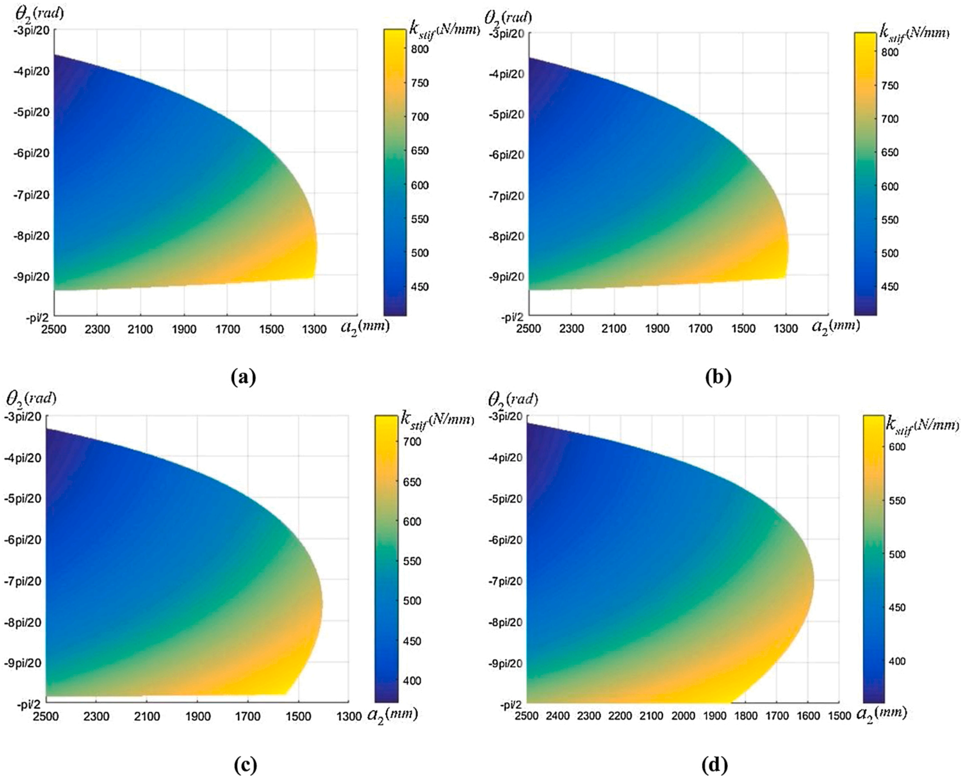

Fig. 5. optimization of θ_2 and a_2,**(a)** $\theta_3 = 0$, **(b)** $\theta_3 = \frac{\pi}{6}$, **(c)** $\theta_3 = \frac{\pi}{4}$, **(d)** $\theta_3 = \frac{\pi}{3}$.

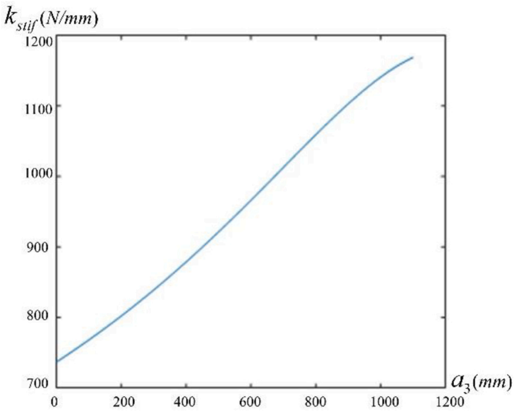

Fig. 6. optimization of a_3 and a_4.

200. It can be obtained from Fig.4 that d_2 and d_3 both have negative influence on system stiffness. In order to get better k_{stif}, d_2 and d_3 should be minimized after meeting the size conditions of the structure. d_2 and d_3 are set to 100 mm in this paper.

3.1.2. *Optimization of θ_2 and a_2*

While optimizing θ_2 and a_2, constraint Eqs. (15) and (16) are added to meet the condition of relative position between PM and SM.

$$a_2\sin(-\theta_2) + (a_3 + a_4)\sin(-\theta_2 + \theta_3) > 2500 \tag{15}$$

$$a_2\cos(\theta_2) + (a_3 + a_4)\cos(\theta_2 + \theta_3) > 1000 \tag{16}$$

From Fig. 5, it can be obtained that the range of the maximum stiffness is almost unchanged when θ_3 changes. The results also shows that: the stiffness value increases with the rising of a_2 and $|\theta_2|$.

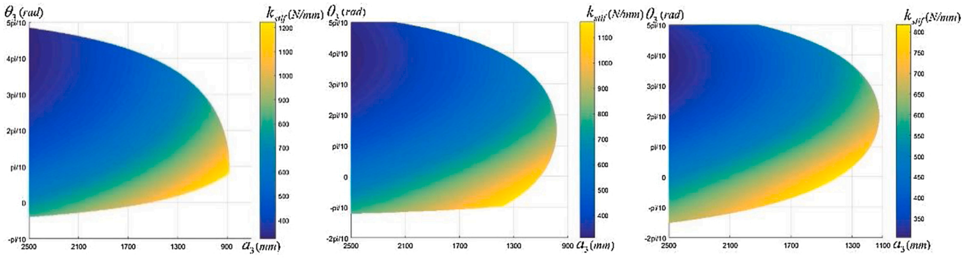

(a) (b) (c)

Fig. 7. optimization of θ_3 and a_3 via θ_2: **(a)** $\theta_2 = -\frac{8\pi}{20}$, **(b)** $\theta_2 = -\frac{7\pi}{20}$, **(c)** $\theta_2 = -\frac{6\pi}{20}$.

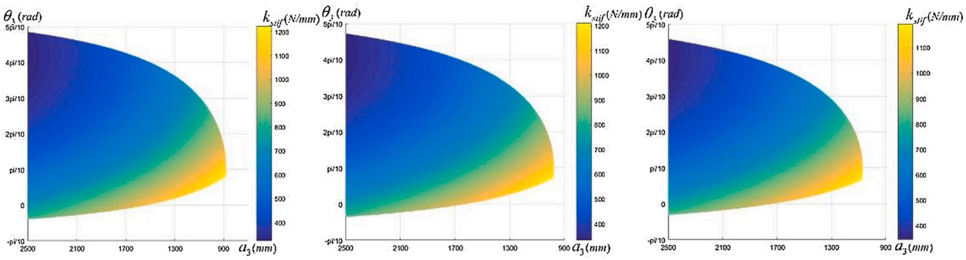

(a) (b) (c)

Fig. 8. optimization of θ_3 and a_3 via a_2: **(a)** $a_2 = 1700$, **(b)** $a_2 = 1600$, **(c)** $a_2 = 1500$.

Table 3
stiffness at $a_2 = 1700$.

θ_2	$-\frac{8\pi}{20}$	$-\frac{23\pi}{60}$	$-\frac{24\pi}{60}$	$-\frac{7\pi}{20}$	$-\frac{\pi}{3}$	$-\frac{19\pi}{60}$	$-\frac{6\pi}{20}$
k_{stif}	1156.36	1170.51	1190.47	1201.38	1186.67	1167.22	1134.04

Table 4
stiffness at $\theta_2 = -\dfrac{7\pi}{20}$.

a_2	1800	1750	1700	1650	1600	1550	1500
k_{stif}	1126.40	1157.65	1201.38	1186.82	1134.26	1114.73	1056.39

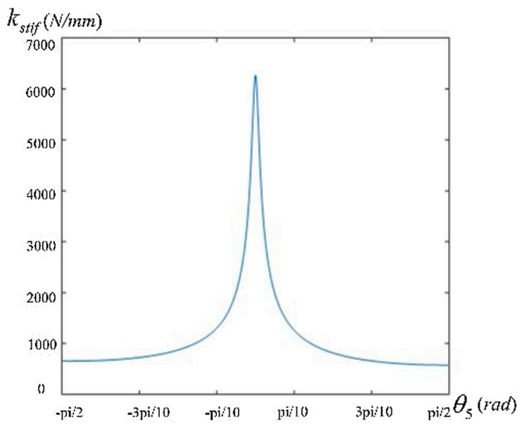

Fig. 9. optimization of θ_5.

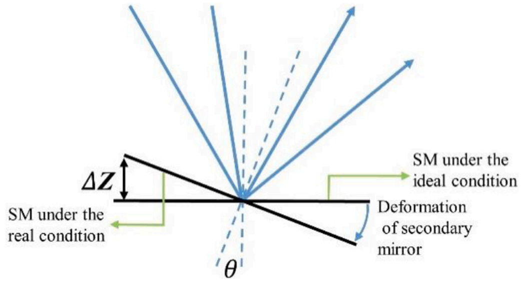

Fig. 10. ΔZ caused by tip and tilt.

The maximum stiffness index can be obtained when θ_2 is between $-\frac{3\pi}{10}$ and $-\frac{2\pi}{5}$ as well as a_2 is between 1500 and 1700.

3.1.3. Optimization of θ_3 and a_3

Because Joint 4 is between a_3 and a_4, the position of J4 needs to be optimized to get better k_{stif} before optimizing θ_3 and a_3.

From Fig. 6, it can be seen that k_{stif} increases when a_3 gets larger, which means better k_{stif} can be obtained when J4 is closed to J5.

The results in Figs. 5 and 6 are used to optimize θ_3 and a_3. In this optimization, a_4 is set to zero. The optimizing object a_3 ranges from 2500 to 1500 and θ_3 ranges from $-\frac{\pi}{2}$ to $\frac{\pi}{2}$.

From Figs. 7 and 8 and Tables 3 and 4, it can be seen that a better k_{stif} can be obtained when $\theta_2 = -\frac{7\pi}{20}$, $a_2 = 1700$. The range of θ_3 is from $\frac{\pi}{10}$ to $\frac{3\pi}{10}$, and the range of a_3 is from 1700 to 1900.

θ_5 is changed from $-\frac{\pi}{2} \sim \frac{\pi}{2}$ using the optimized parameters from above. It can be seen from Fig. 9 that if θ_5 is controlled to the range of $-\frac{\pi}{40} \sim \frac{\pi}{40}$, k_{stif} will be more than 3000 N/mm.

3.2. Calculation of parallel compliance matrix

Parallel mechanism of the truss structure is shown in Fig. 1. The 3-6R structure is composed of 3 same limbs. C_1, C_2, C_3 are compliance matrix of the EE. C_2, C_3 can be obtained through the transmission matrix.

$$C_2 = T_{\frac{2\pi}{3}} \cdot C_1 \cdot T_{\frac{2\pi}{3}}^T \tag{17}$$

$$C_3 = T_{\frac{4\pi}{3}} C_1 T_{\frac{4\pi}{3}}^T \tag{18}$$

In the equation, $T_{\frac{2\pi}{3}}$, $T_{\frac{4\pi}{3}}$ are the transmission matrix

$$T_{\frac{2\pi}{3}} = \begin{bmatrix} \cos\frac{2\pi}{3} & -\sin\frac{2\pi}{3} & 0 \\ \sin\frac{2\pi}{3} & \cos\frac{2\pi}{3} & 0 \\ 0 & 0 & 1 \end{bmatrix} \tag{19}$$

$$T_{\frac{4\pi}{3}} = \begin{bmatrix} \cos\frac{4\pi}{3} & -\sin\frac{4\pi}{3} & 0 \\ \sin\frac{4\pi}{3} & \cos\frac{4\pi}{3} & 0 \\ 0 & 0 & 1 \end{bmatrix} \tag{20}$$

Thus, the parallel flexibility matrix of the structure is

$$C_{tt} = \left(C_{tt1}^{-1} + C_{tt2}^{-1} + C_{tt3}^{-1}\right)^{-1} \tag{21}$$

$$C_{tr} = \left(C_{tr1}^{-1} + C_{tr2}^{-1} + C_{tr3}^{-1}\right)^{-1} \tag{22}$$

Then,

$$C_{tt}\text{'} = \begin{bmatrix} 2.62003\text{e-}4 & 9.851853\text{e-}5 & 3.55928\text{e-}4 \\ 9.85185\text{e-}5 & 1.78827\text{e-}3 & -7.15779\text{e-}5 \\ 3.55928\text{e-}4 & -7.15779\text{e-}5 & 1.49788\text{e-}3 \end{bmatrix} \quad C_{tr}\text{'} = \begin{bmatrix} 2.01576\text{e-}8 & -1.93230\text{e-}7 & 2.77446\text{e-}8 \\ 3.88870\text{e-}7 & 0 & 6.88193\text{e-}7 \\ -1.46454\text{e-}8 & -1.29434\text{e-}6 & -2.01576\text{e-}8 \end{bmatrix}$$

Table 5
deformations and wavefront aberrations caused by gravity.

	$Z_{\max}(mm)$	$Z_{\min}(mm)$	$\Delta Z(mm)$	$LS(nm)$
$e_f = [0,0,1]^T$	1.49856e-3	1.49719e-3	1.37234e-6	27.4467
$e_f = [1,0,0]^T$	3.56316e-4	3.55540e-4	7.76540e-7	15.5308

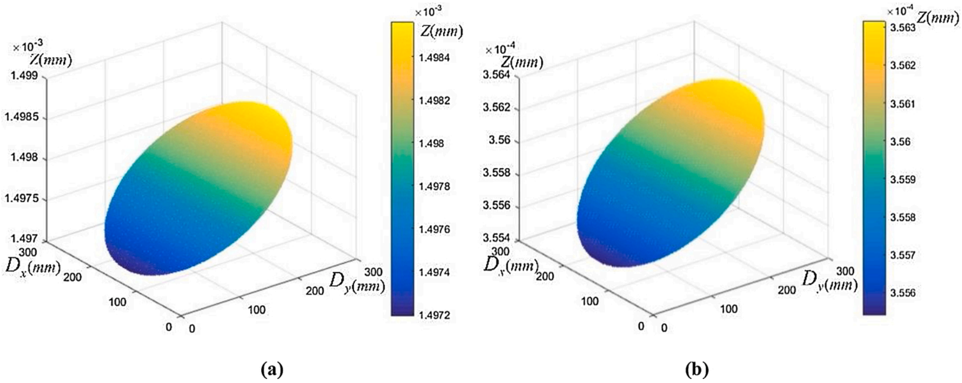

Fig. 11. Aberrations caused by deformations in gravity**(a)** gravity parallel to the z-axis**(b)** gravity parallel to the x-axis.

Table 6
Non-optimized deformations and wavefront aberrations caused by gravity ($e_f = [0,0,1]^T$).

a_3	$Z_{\max}(mm)$	$Z_{\min}(mm)$	$\Delta Z(mm)$	$LS(nm)$
2300	3.7200e-03	3.7159e-03	4.0930e-06	81.8597
2100	3.2129e-03	3.2091e-03	3.8914e-06	77.8277
1900	2.7476e-03	2.7439e-03	3.6897e-06	73.7937

Table 7
Non-optimized deformations and wavefront aberrations caused by gravity ($e_f = [1,0,0]^T$).

a_3	$Z_{\max}(mm)$	$Z_{\min}(mm)$	$\Delta Z(mm)$	$LS(nm)$
2300	3.4122e-03	3.4091e-03	3.1369e-06	62.7378
2100	2.8940e-03	2.8910e-03	2.9904e-06	59.8078
1900	2.4175e-03	2.4147e-03	2.8439e-06	56.8778

3.3. Wavefront aberrations verification by Zernike polynomials

After the compliance matrix is obtained, deformation of the SM in different gravities can be calculated by TEI and REI. Deformation along each direction is calculated by decomposing TEI and REI. Due to analyzing the rigid body deformation of the SM, only piston, tip and tilt are considered in this paper. First three order aberrations will be obtained after the result is measured by Zernike polynomials. Finally, the value of deviation is compared with the system error requirement.

Because the value of θ caused by ΔZ is small enough in Fig.10, $\sin\theta = \theta$. The aberration caused by ΔZ can be written as $LS = \theta \cdot f = \frac{\Delta Z}{D/2} \cdot f$. ΔZ is the deformation calculated by TEI and REI, LS is the aberrations caused by ΔZ. D is the diameter of the SM, f is the distance from SM to the image plane of the optical system. According to the results shown in Table 5, the rigid deformations of the secondary mirror are 27.4467 nm and 15.5308 nm under gravity along z-axis and x-axis separately. The result meets the aberration requirement, which means the optimization meets the requirement of the telescope system (Fig. 11).

In order to verify the result, three sets of data in θ_3 optimization are calculated to compare with the optimized result. θ_3 is set to $\frac{3\pi}{10}$, a_3 is set to 2300, 2100, 1900 separately. According to Tables 6 and 7, the aberrations produced by the optimized parameters are much smaller than the aberrations caused by the non-optimized parameters. This comparison shows that posture optimization has great effect on reducing the error.

4. Conclusion

A new truss based on robotics is proposed in this paper to solve the over-height problem and the diameters of vehicle-mobile telescopes are raised to 2 m scale. After the basic structure form is confirmed, the posture of the structure is optimized by k_{stif}. The workspace restrictions are added in posture optimization, so the dimensions can be obtained. TEI and REI are raised and established relationship with wavefront aberrations through Zernike polynomials. e_f can be changed to simulate the gravity of the telescope and different states are calculated while the telescope is working. Rigid deformations of the secondary mirror are 27.4467 nm and 15.5308 nm in gravity with different orientations, which is verified to meet the error requirement with the optimized parameters. The structure is proved to have implementation after the error and stiffness verifications.

Declaration of Competing Interest

The authors reported no declarations of interest.

Acknowledgements

This work is supported by Youth Science Foundation of the Chinese Academy of Sciences (CAS) (No. 11803035), the Youth Innovation Promotion Association CAS (No. 2020221) and the Norman Bethune Medical engineering and equipment center under Grant BQEGCZX2019042.

References

[1] D. Yu, The Rayleigh criterion, in: D. Yu (Ed.), Engineering Optics, China Machine Press, China, 2013, pp. 204–206.
[2] W. Sutherland, J. Emerson, G. Dalton, E. Atadettedgui, S. Beard, R. Bennett, et al., The visible and infrared survey telescope for astronomy (VISTA): design, technical overview, and performance, Astron. Astrophys. 575 (2014). A25(1)- A25(27).
[3] V. Ford, C. Carter, C. Delrez, P. Fumi, E. Gabriel, D. Gallieni, Jitter studies for the secondary and tertiary mirror systems on the thirty Meter Telescope, SPIE Astronomical Telescopes+Instrumentation 9151 (2014), 91512H (1)-91512H (15).
[4] Z. Nan, C. Li, G. Wei, Z.X. Song, Z. Chao, G.R. Ren, et al., A secondary mirror adjustment system with hexapod structure for optical telescope application, SPIE Society of Photo-optical Instrumentation Engineers 9280 (2014), 92800N-1-92800N-7.
[5] S. Psilodimitrakopoulos, L. Mouchliadis, I. Paradisanos, A. Lemonis, G. Kioseoglou, E. Stratakis, Ultrahigh-resolution nonlinear optical imaging of the armchair orientation in 2D transition metal dichalcogenides, Light Sci. Appl. 7 (2018) 1–9.
[6] R. Kammel, R. Ackermann, J. Thomas, J. Gotte, S. Skupin, A. Tunnermann, S. Nolte, Enhancing precision in fs-laser material processing by simultaneous spatial and temporal focusing, Light Sci. Appl. 3 (2014) 1–8.
[7] C. Hu, J. Liu, J. Wang, Z. Gu, C. Li, Q. Li, Y. Li, S. Zhang, C. Bi, X. Fan, W. Zheng, New design for highly durable infrared-reflective coatings, Light Sci. Appl. 7 (2018) 1–11.
[8] C. Atkinson, S. Texter, Status of the JWST optical telescope element, SPIE Astronomical Telescopes+Instrumentation 6265 (2006) 1–10.
[9] B. Hu, Y. Lu, Solving stiffness and deformation of a 3-UPU parallel manipulator with one translation and two rotations, Robotica 29 (2011) 815–822.
[10] M. Wang, H. Liu, T. Huang, Derek G. Chetwyndc, Compliance analysis of a 3-SPR parallel mechanism with consideration of gravity, Mech. Mach. Theory 84 (2015) 99–112.
[11] G. Cheng, P. Xu, D. Yang, et al., Stiffness analysis of a 3CPS parallel manipulator for mirror active adjusting platform in segmented telescope, Robotics Computer Integrated Manuf. 29 (2013) 302–311.
[12] Y. Li, E. Zhang, Y. Song, Z. Feng, Stiffness modeling and analysis of a novel 4-DOF PKM for manufacturing large components, Chin. J. Aeronaut 26 (2013) 1577–1585.
[13] G. Xiong, Y. Ding, L. Zhu, Stiffness-based pose optimization of an industrial robot for five-axis milling, Robotics Computer Integrated Manuf. 55 (2019) 19–28.
[14] M. Cordes, W. Hintze, Offline simulation of path deviation due to joint compliance and hysteresis for robot machining, Int. J. Adv. Manuf. Technol. 90 (2016) 1–9.
[15] T. Sun, B. Lian, Stiffness and mass optimization of parallel kinematic machine, Mech. Mach. Theory 120 (2018) 73–88.
[16] B. Lian, T. Sun, Y.M. Song, Parameter sensitivity analysis of a 5-dof parallel manipulator, Robotics Computer Integrated Manuf. 46 (2017) 1–14.
[17] J.K. Salisbury, Active stiffness control of a manipulator in Cartesian coordinates, Proceedings of the 19th IEEE Conference on Decision and Control, Albuquerque, NM (1980) 87–97.
[18] S.-F. Chen, I. Kao, Conservative congruence transformation for joint and Cartesian stiffness matrices of robotic hands and fingers, Int. J. Robot. Res 19 (2000) 835–847.
[19] E. Abele, M. Weigold, S. Rothenbucher, Modeling and identification of an industrial robot for machining applications, Ann. CIRP 56 (2007) 387–390.
[20] J. Angeles, On the nature of the Cartesian stiffness matrix, Ingenieria Mecanica Tecnologia Ydesarrollo 3 (2010) 163–170.
[21] S.H.H. Zargarbashi, W. Khan, J. Angeles, Posture optimization in robot-assisted machining operations, Mech. Mach. Theory 51 (2012) 74–86.
[22] Y. Guo, H. Dong, Y. Ke, Stiffness-oriented posture optimization in robotic machining applications, Robotics Computer Integrated Manuf. 35 (2015) 69–76.
[23] R.R. Shannon, J.C. Wyant, Applied Optics and Optical Engineering, XI, Academic Press, New York, USA, 1992, pp. 55–60.
[24] F. Zernike, How I discovered phase contrast, Science 121 (1955) 345–349.
[25] C. Dumas, S. Caro, S. Garnier, B. Furet, Joint stiffness identification of six-revolute industrial serial robots, Robotics Computer Integrated Manuf. 27 (2011) 881–888.
[26] Y. Lin, H. Zhao, H. Ding, Posture optimization methodology of 6R industrial robots for machining using performance evaluation indexes, Robotics Computer Integrated Manuf. 48 (2017) 59–72.
[27] F. Wang, Q. An, Y. Fei, Evaluation of the mirror surface figure error based on the SlopeRMS, Optik 127 (2016) 39–42.
[28] X. Liu, X. Tian, Z. Wang, Lightweight design of high volume SiC/Al composite mirror for remote camera, Optik 188 (2019) 64–70.